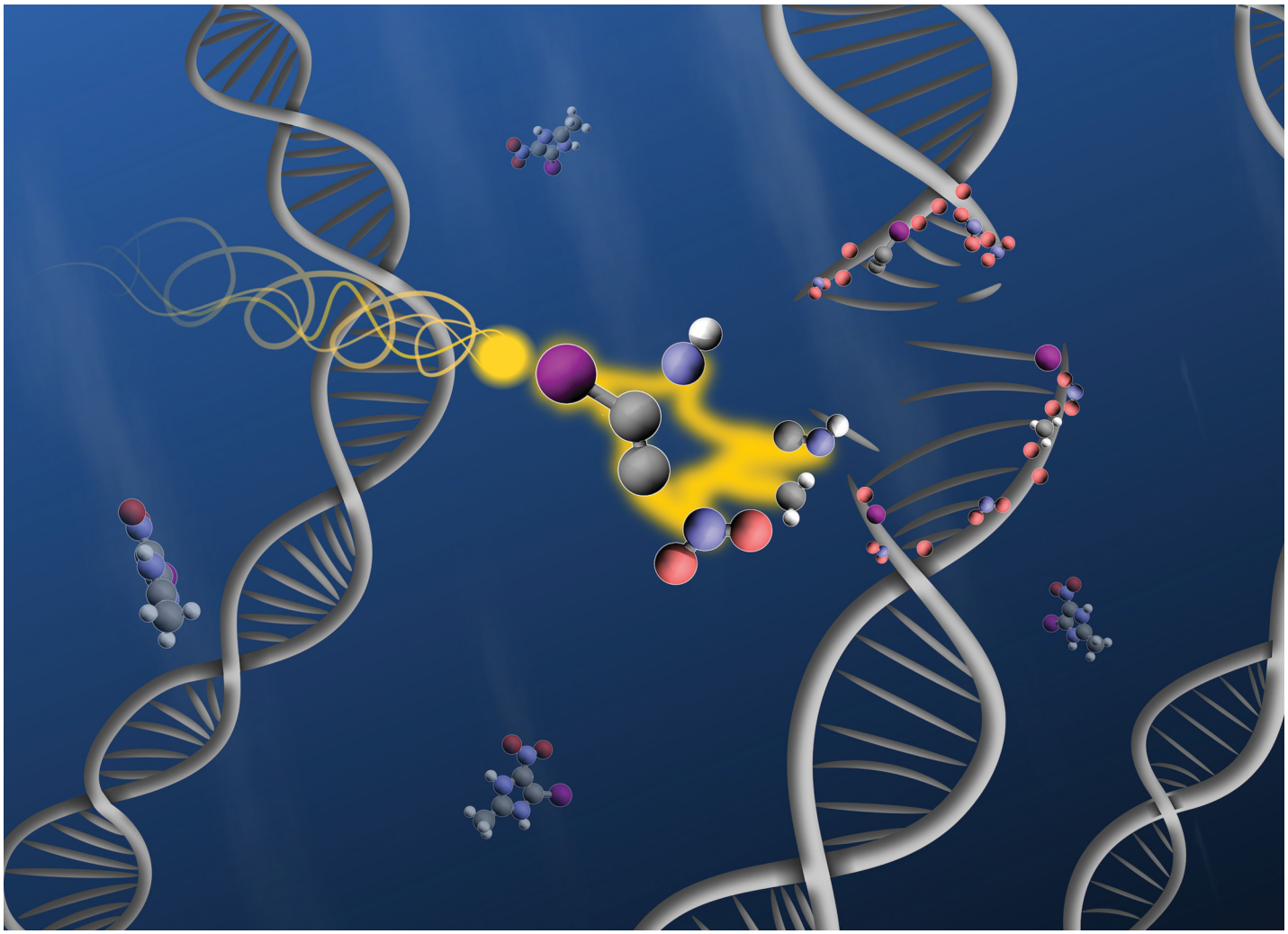

**Showcasing research from workers in the Biophysics group at the Institution of Physics and Astronomy at Uppsala University, and from the Institute of Physics, University of Tartu.**

Heavy element incorporation in nitroimidazole radiosensitizers: molecular-level insights into fragmentation dynamics

Radiation damage occurs on the molecular level. By analyzing the fragmentation of radiosensitizers with mass spectrometry and quantum mechanical calculations, one can get valuable physiobiological insights into their potential role in radiotherapy. We have studied the fragmentation of nitroimidazole-based sensitizers functionalized with heavy elements. The idea is to enhance the absorption cross-section of the nitroimidazoles to increase the generation of fragments important for DNA double-strand breaks.

## As featured in:


See Pamela H. W. Svensson, Marta Berholts *et al.*, *Phys. Chem. Chem. Phys.*, 2024, **26**, 770.

ROYAL SOCIETY OF CHEMISTRY

rsc.li/pccp

Registered charity number: 207890

PCCP Owner Societies

PCCP

ROYAL SOCIETY OF CHEMISTRY

PAPER

View Article Online
View Journal | View Issue



Cite this: *Phys. Chem. Chem. Phys.*, 2024, **26**, 770

# Heavy element incorporation in nitroimidazole radiosensitizers: molecular-level insights into fragmentation dynamics†

Pamela H. W. Svensson, *[a] Lucas Schwob,[b] Oscar Grånäs,[a] Isaak Unger,[a] Olle Björneholm,[a] Nicusor Timneanu,[a] Rebecka Lindblad,[a] Anna-Lydia Vieli,[a] Vicente Zamudio-Bayer,[c] Martin Timm,[c] Konstantin Hirsch,[c] Carl Caleman[ad] and Marta Berholts *[e]

Received 9th August 2023,
Accepted 16th October 2023

DOI: 10.1039/d3cp03800a

rsc.li/pccp

The present study investigates the photofragmentation behavior of iodine-enhanced nitroimidazole-based radiosensitizer model compounds in their protonated form using near-edge X-ray absorption mass spectrometry and quantum mechanical calculations. These molecules possess dual functionality: improved photoabsorption capabilities and the ability to generate species that are relevant to cancer sensitization upon photofragmentation. Four samples were investigated by scanning the generated fragments in the energy regions around C 1s, N 1s, O 1s, and I 3d-edges with a particular focus on $NO_2^+$ production. The experimental summed ion yield spectra are explained using the theoretical near-edge X-ray absorption fine structure spectrum based on density functional theory. Born–Oppenheimer-based molecular dynamics simulations were performed to investigate the fragmentation processes.



## 1 Introduction

In radiation therapy with X-rays, the damage is mediated to the DNA directly by ionization and indirectly through reactive species formed upon the ionization of water. Here, about two-thirds of all biological damage results from indirect action, while direct effects deal just one-third of the damage.[1] The primary objective of radiotherapy is to maximize the dose delivered to the target tumor tissue while minimizing damage to surrounding healthy tissue. One approach to achieving this is through the use of radiosensitizers, which increase the sensitivity of tumor tissue to radiation treatment. The effectiveness of a radiosensitizer is determined by the ratio of the radiation dose required to produce a given biological effect without the radiosensitizer compared to the dose required in its presence. In the treatment of low oxygenated tissue called hypoxia, often found in tumors, nitroimidazoles attracted significant interest.[2–5] Nitroimidazoles are a class of electrophilic radiosensitizers. These compounds mimic oxygen actions in radiotherapy and their radiosensitization efficacy was linked to the quantity of NO and/or $NO_2$ fragments generated during ionization.[6–8] The fragmentation products of nitroimidazoles, in the same way as oxygen, can attach to DNA radicals formed by ionizing radiation or secondary electrons. This can disrupt DNA repair processes and result in increased DNA damage. This effect is beneficial in radiotherapy as it allows for lower doses of radiation and thus reduces the associated side effects.[4,5,7] Additionally, NO was shown to help with the oxygenation of the hypoxic cells.[9]

Despite ongoing investigations of numerous radiosensitizer compounds, interpreting clinical trial results in the context of underlying physical and chemical processes remains challenging. This has hindered the ability to fully comprehend why some radiosensitizers are more effective than others. Therefore, the precise mechanism underlying sensitization is not yet fully understood.

The goal of this study is to investigate on the molecular level how nitroimidazole-based model compounds respond to ionizing radiation by applying near-edge X-ray mass spectrometry (NEXAMS) and quantum mechanical calculations. In the experiment, a heavy element, iodine, was incorporated into nitroimidazoles. The studied molecules are 4-iodo-2-methyl-5-nitroimidazole (INim), 1-ethyl-5-iodo-2-methyl-4-nitroimidazole (EtINim), 2-bromo-5-iodo-4-nitroimidazole (BrINim), and non-iodinated reference

[a] *Department of Physics and Astronomy, University of Uppsala, SE-75120 Uppsala, Sweden. E-mail: pamela.svensson@physics.uu.se*
[b] *Deutsches Elektronen-Synchrotron DESY, Notkestr. 85, 22607 Hamburg, Germany*
[c] *Abteilung für Hochempfindliche Röntgenspektroskopie, Helmholtz Zentrum Berlin für Materialien und Energie, 12489 Berlin-Adlershof, Germany*
[d] *Center for Free-Electron Laser Science, DESY, DE-22607 Hamburg, Germany*
[e] *Institute of Physics, University of Tartu, W. Ostwald 1, EST-50411, Tartu, Estonia. E-mail: marta.berholts@gmail.com*

† Electronic supplementary information (ESI) available. See DOI: https://doi.org/10.1039/d3cp03800a

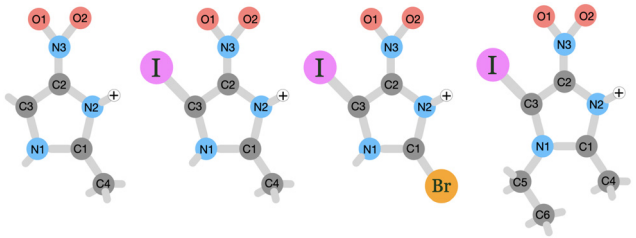


Fig. 1 Schematic picture of the studied protonated molecules. From left to right: $NimH^+$, $INimH^+$, $BrINimH^+$, and $EtINimH^+$.

2-methyl-5-nitroimidazole (Nim). The structures of their protonated forms with initial charge +1, as they appear after electrospray ionization, are presented in Fig. 1. The location of the proton was assigned to the N2 site due to its higher proton affinity.[10] We change the structure of the non-iodinated sample, referred to as $NimH^+$ by introducing an iodine atom to the C3 site, resulting in $INimH^+$. In addition, there are two variations of $INimH^+$: one involves replacing the methyl group at the C1 site with a bromine atom ($BrINimH^+$), while the other includes adding an ethyl chain to the N1 site ($EtINimH^+$). The purpose of iodine, a high-*Z* element, is to act as an "antenna" for X-rays during medical irradiation. Specifically, the high photoionization cross section of iodine is exploited to enhance the X-ray absorption efficiency of the nitroimidazoles. The expected net result is twofold: the iodine absorption hotspot locally enhances the radiation dose by generating secondary X-rays, photo- and Auger electrons, all important for efficient DNA strand breaks,[11] while nitroimidazole counterpart produces sensitization-relevant species upon fragmentation. In this work, we focus on the latter. The study of the fragmentation of iodinated nitroimidazoles is motivated by promising *in vitro* results where iodinated samples exhibited better radiosensitization of hypoxic cells at much lower concentrations than their iodine-free ref. 12. The positive effect of localized radiation dose enhancement with iodine in tumors was observed significantly earlier.[13,14]

Multiple studies have examined the photoionization and photofragmentation of various isolated nitroimidazoles using techniques such as X-ray photoelectron spectroscopy,[15–18] near-edge X-ray absorption fine structure (NEXAFS) spectroscopy,[18,19] multiparticle coincidence spectroscopy,[16,17,20–24] and mass spectrometry.[10,16,17,23,25–29] However, there is a lack of similar investigations specifically focused on halogenated nitroimidazoles, except for a recent study on the gas-phase fragmentation of neutral brominated nitroimidazoles using multiparticle coincidence technique.[30] This study demonstrated that the bromination of nitroimidazoles is an effective way of introducing dual functionality to the radiosensitizer model compounds. Notably, the addition of a bromine atom resulted in significant production of reactive $Br^+$ ions and a modest decrease of approximately 15% in the release of nitro group-related species upon dissociation at the C 1s, N 1s, and Br 3d edges. This is in stark contrast to the significant impact of methylation at the N1 site, which reduces the amount of $NO^+/NO_2^+$ species by approximately 90%.[20,22] In this study, we extend the investigations on the fragmentation of halogenated nitroimidazoles to another halogen atom – iodine. Iodine's deeper 1s edge (33.17 keV) compared to bromine (13.47 keV) allows it to absorb higher energy X-rays, potentially leading to more precise radiation delivery to tumor tissues and more energetic Auger electron production causing additional local damage.[31] This advantage is particularly beneficial in low-energy radiation treatments like superficial and orthovoltage radiotherapy,[32] as well as emerging synchrotron radiation-based photon activation therapies with a focus on low-energy X-rays.[33]

Here, we explore the influence of the electronic structure of chosen samples on their fragmentation following core excitation and ionization around C 1s, N 1s, O 1s, and I 3d-edges, therefore imitating the dominant secondary processes of X-ray therapy. We focus on the question of whether the incorporation of iodine, affects the electronic environment and thus the production of sensitization-relevant fragments at different photon energies.

## 2 Method

### 2.1 Experiment

The near-edge X-ray absorption mass spectrometry (NEXAMS) experiment was performed at the BESSY II synchrotron facility using UE52_PGM beamline with the Ion Trap end-station (Berlin, Germany).[34] The samples were introduced into the gas phase by an electrospray ionization (ESI) source in a singly protonated form. A radio frequency ion funnel was used for accumulating and focusing created ions. Next, the ion beam was guided through two consecutive radio frequency hexapole ion guides to a quadrupole mass filter. The mass filter was optimized to let through exclusively protonated parent molecules deflecting ions with lower and higher mass-to-charge ratios ($m/z$). After that, the ions were sent to the 90° angle deflector for removal of neutral particles from the ion beam. Finally, the protonated parent ions entered the cryogenic linear trap through another quadrupole ion guide. In the trap, ions were irradiated with linearly polarized X-rays in the horizontal direction producing fragments that were then analyzed by a high-transmission reflectron time-of-flight mass spectrometer (RTOF). The nominal $m/z$ range of the spectrometer is about 2–2500. The trap was optimized for fragments in the $m/z$ range of about 38–130, while the parent protonated molecules had $m/z$ of 128 ($NimH^+$), 254 ($INimH^+$), 282 ($EtINimH^+$), and 319 ($BrINimH^+$). This range was selected to have both $NO_2^+$ ($m/z$ 46) and $I^+$ ($m/z$ 127) ions present in the mass spectra. No fragments were detected outside of the optimized range. The photon flux was in the order of $10^{13}$ ph. $s^{-1}$.

The samples INim, EtINim, BrINim, and Nim were purchased from BLD Pharmatech with 95+%, 97%, 97%, and 99.8% purity, correspondingly. The samples were received in powder form and injected into the experimental chamber from their highly diluted solutions. First, a 5 mM stock solution was prepared with a 1 : 1 ratio of water to methanol. Then, 0.1 ml of the stock solution was dissolved in water to reach 98 μM concentration. This solution was then injected through an ESI source into the experimental chamber with a constant flow rate of 0.2 ml $h^{-1}$.

The mass spectra were measured for all samples in their protonated forms across C 1s (275–300 eV), N 1s (395–430 eV), and O 1s (527–542 eV) near-edge regions with 0.1 eV step and 10–15 s acquisition time per step. For iodinated samples also I 3d edge (615–690 eV) was scanned with 0.2 eV step and 10–20 s acquisition time per step. Exceptions apply for the C 1s and N 1s measurements of the $INimH^+$. These measurements were recorded using a narrower photon energy window, specifically 283–298 eV for C 1s and 397–417 eV for N 1s. At the start of the photon energy scans, photon bandwidth at FWHM was 145 meV for C 1s, 250 meV for N 1s, 256 meV for O 1s, and 325 meV for I 3d. The background mass spectrum without X-rays was measured for each scan to be subtracted from the recorded mass spectra. The mass spectra taken at different photon energies were normalized by the photocurrent measured with a calibrated GaAsP diode.

Data was analyzed using custom-made macros in Igor Pro software. Partial ion yield spectra were constructed from the TOF spectra measured as a function of the photon energy for each fragment by integrating the points within a small TOF window containing the peak of interest. The total NEXAMS spectrum is a sum of all the partial ion yield spectra and is an approximation to the total ion yield spectrum.

### 2.2 Theory

To better understand the electronic structure and fragmentation processes of the studied molecules, Density Functional Theory (DFT) has been used to simulate both NEXAFS spectra and Molecular Dynamics after photoionization. In order to accurately replicate the NEXAFS spectra for the different systems, a geometry optimization was performed using the B3LYP[35] functional and def2-TZVPP relativistic basis sets for N, C, H, O, and Br atoms as implemented in the ORCA software.[36] I atoms were separately described using the segmented all-electron relativistically contracted (SARC) basis sets with zeroth-order regular approximation (ZORA).[37] By employing the TD-DFT[38] method we evaluated the transition energies from the C 1s orbital (for all samples) and the N 1s orbital (for $NimH^+$ and $INimH^+$) to all available excited states. Transition probabilities were calculated using the response of the perturbed electron density to electromagnetic radiation within the TD-DFT theory in the ORCA package. The spectra of each chemically distinct atom were individually calculated and then summed to obtain the total spectrum. Subsequently, the total spectrum was adjusted to align with the most prominent characteristics observed in the experimental spectrum.

In addition to the NEXAFS calculations, we have performed Born–Oppenheimer molecular dynamics simulations using the Siesta code[39] to understand the fragmentation process after photoionization. We have previously employed this methodology in various contexts, including theoretical investigations,[40,41] as well as in studies where we compared our simulation results with experimental data.[42–44] From the comparison between simulations and the experiment, we could conclude that the relaxation time scales are short enough for the fragmentation to be dominated by the electronic structure of the ground-state geometry.[42] This motivates us to use the same approach in the present study. To describe the exchange and correlation effect we used the functional generalized gradient approximation (GGA) as described by Perdew, Burke, and Ernzerhof, and the atomic orbitals were described using Norm-conserving pseudopotentials for all the molecules studied.[45,46]

As a first step, we conducted a 1 ns simulation in a vacuum environment using the Verlet algorithm. Subsequently, 20 structures were selected from this simulation and utilized as starting geometries for the production run. In the calculations, we focused on the ionization processes dominant during radiotherapy. We studied fragmentation of the INimH with a charge of +3, +4, and +5 possible after ionization and subsequent Auger decay and cascaded Auger decay. The fragmentation of the non-iodinated NimH was studied for the charge +3. During the simulation, we tracked the movement of each atom while allowing the molecules to decompose into fragments over a period of 1 ps with the integration step of 0.5 fs, providing sufficient time for the molecular dynamics to capture the evolution of the system. To determine the breaking point of a bond, we employed the Bond Integrity parameter, which was defined in an earlier study.[44] By including the bond distance between atoms and their deviation using the mean bond distances and standard deviation from thermalization runs, one can obtain a value between 0 and 1. A bond can be considered broken if the bond integrity reaches 0.

## 3 Results

### 3.1 Summed mass spectra

The mass spectra of the four studied molecules, recorded across the C 1s, N 1s, O 1s, and I 3d edges, are depicted in Fig. 2. For detailed information about the photon energy ranges employed in the measurements, please refer to Section 2.1. To facilitate comparison, a mass spectrum measured at a lower photon energy of 110 eV (upon non-resonant photon absorption in the valence levels) is also included. The summed mass spectra recorded across the above-mentioned edges show minimal fluctuations in resulting fragments within each sample despite variations in the photon energy and therefore in the absorption sites. These fluctuations are primarily observed as slight variations in the intensity of certain fragments. The most significant changes are observed in the mass spectra measured at the photon energy of 110 eV. Here, a notable increase of $I^{++}$ at $m/z$ 63.5 is detected for all iodinated samples and especially for $BrINimH^+$ and $INimH^+$.

Across all spectra, a prominent $NO_2^+$ fragment at $m/z$ 46 is observed, accompanied by two sets of peaks clustered around $m/z$ 38–43 and $m/z$ 50–55. For $INimH^+$ and $BrINimH^+$, the second set ends at $m/z$ 54. We attribute these peaks to the ions formed upon the fragmentation of the imidazole ring (see Table 1 for the assignments). In the mass spectra of $BrINimH^+$, there are additional peaks in the lower $m/z$ region attributed to $Br^{++}$ isotopes at $m/z$ 39.5 and $m/z$ 40.5. The brominated sample has also other Br-containing fragments such as $Br^+$ at $m/z$ 79

 

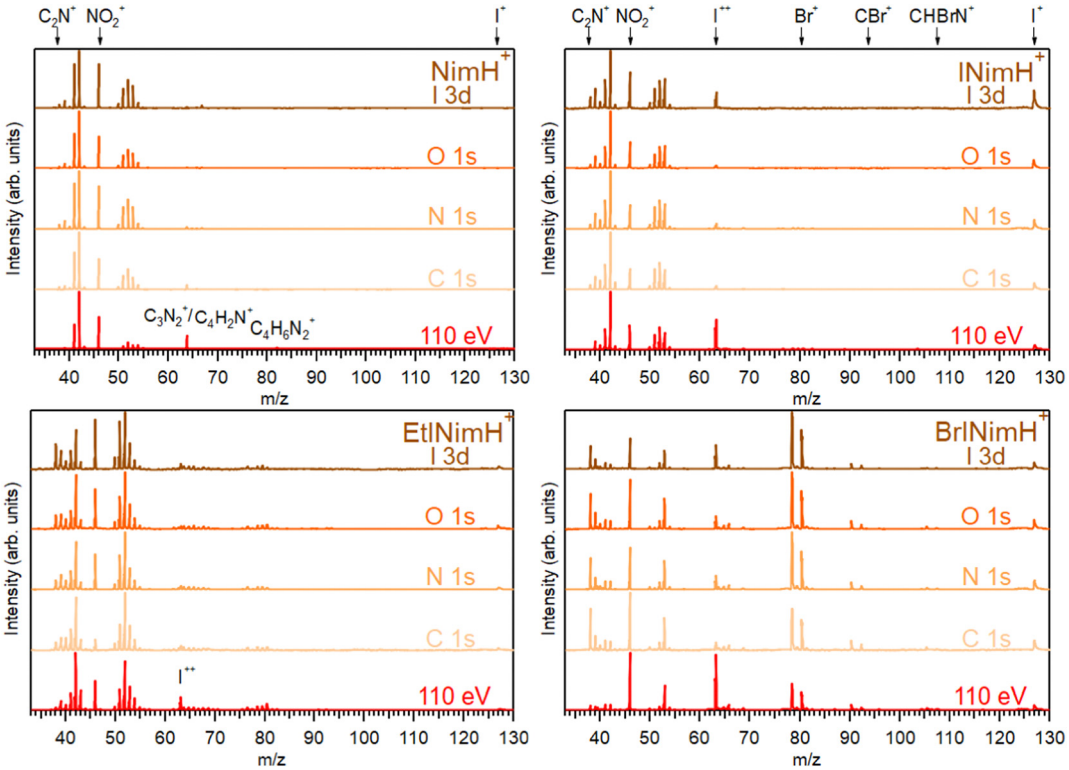


Fig. 2 Summed mass spectra of studied samples measured across C 1s, N 1s, O 1s, and I 3d edges. Additionally, mass spectra taken at 110 eV photon energy are shown. All spectra were normalized to the most abundant ion in the particular spectrum.

and 81, $HBr^+$ at *m*/*z* 80 and 82, $CBr^+$ at *m*/*z* 91 and 93, and $CHBrN^+$ at *m*/*z* 106 and 108 easily identified due to the approximately 1 : 1 bromine isotope ratio. All iodinated samples contain $I^+$ at *m*/*z* 127 and $I^{++}$ at *m*/*z* 63.5 in their mass spectra.

The non-iodinated sample, $NimH^+$, has a peak at *m*/*z* 64 that corresponds to $C_3N_2^+$ or/and $C_4H_2N^+$ and a weak peak at *m*/*z* 82 that we attribute to the parent fragment that has lost $NO_2$. The corresponding signal of the parent-$NO_2$ is not visible in the mass spectra of other samples due to the limited mass range explained by the ion trap settings. In the mass spectrum of $EtINimH^+$, there are weak peaks present at the higher *m*/*z* 76–81. These peaks arise due to the presence of an ethyl group attached to the nitroimidazole ring. Consequently, upon fragmentation of the ring, heavier carbon-containing fragments are produced (see Table 1).

The most straightforward way to investigate the influence of the iodine addition on the fragmentation is to compare $NimH^+$ and $INimH^+$ samples as these structures are chemically equivalent except for one iodine atom on the latter. The biggest difference is the presence of $I^+$ and $I^{++}$ ions in the mass spectrum of $INimH^+$. There are subtle differences in the ratios of the peaks located on the left and right sides of the $NO_2^+$. Nevertheless, a peak at *m*/*z* 42, that could be assigned to $C_2H_4N^+$, $CH_2N_2^+$, and/or $CNO^+$ ions, remains dominant for both samples. Please note that for $NimH^+$ and $INimH^+$, this peak was solely assigned to $C_2H_4N^+$ according to our calculations (see Table 2). The peak at *m*/*z* 46 ($NO_2^+$) is less intense for the $INimH^+$ in comparison with the dominant peak but becomes stronger at the highest photon energy, copying the behavior of $NimH^+$ (see a mass spectrum recorded at I 3d edge in Fig. 2). The peak at *m*/*z* 41, which we assign to the $C_2H_3N^+$ and/or $CHN_2^+$ ions, becomes weaker in the case of the iodinated sample. Other than that, the distribution of the ions remains largely unchanged meaning that the addition of iodine does not drastically alter the fragmentation outcome, apart from adding $I^+$ and $I^{++}$ ions and lowering the $NO_2^+$ ions production.

### 3.2 NEXAMS spectra and $NO_2^+$ production

In Section 3.1, the mass spectra demonstrated the summed results obtained across all the measured edges. To gain a deeper understanding of the photon energy-dependent behavior of the produced fragments and examine the possibility of enhancing or inhibiting the production of sensitization-relevant $NO_2^+$ ions at specific photon energies, we now focus on the description of the NEXAMS spectra and partial ion yield curves with an emphasis on $NO_2^+$ production.

Fig. 3 depicts NEXAMS spectra measured for $EtINimH^+$ as an example (see shaded spectra at the bottom) and branching fraction of $NO_2^+$ ions for all samples across measured edges. According to the figure, a non-iodinated molecule, $NimH^+$, consistently produces the largest amount of $NO_2^+$ ions at all photon energies measured. The percentage varies at different edges and on average grows from C 1s to I 3d from 14% to 18%. Iodinated samples, on the other hand, exhibit similar $NO_2^+$ yields, which are approximately 50% lower than that of $NimH^+$

Table 1 Identification of the detected ions in the experiments (see Fig. 2)

| $m/z$ | $NimH^+$ | $INimH^+$ | $EtINimH^+$ | $BrINimH^+$ |
|---|---|---|---|---|
| 38 | $C_2N^+$ | $C_2N^+$ | $C_2N^+$ | $C_2N^+$ |
| 39 | $C_2HN^+$ | $C_2HN^+$ | $C_2HN^+$ | $C_2HN^+$ |
| 39.5 | — | — | — | $^{79}Br^{++}$ |
| 40 | $C_2H_2N^+/CN_2^+$ | $C_2H_2N^+/CN_2^+$ | $C_2H_2N^+/CN_2^+$ | $C_2H_2N^+/CN_2^+$ |
| 40.5 | — | — | — | $^{81}Br^{++}$ |
| 41 | $C_2H_3N^+/CHN_2^+$ | $C_2H_3N^+/CHN_2^+$ | $C_2H_3N^+/CHN_2^+$ | $CHN_2^+$ |
| 42 | $C_2H_4N^+/CH_2N_2^+/CNO^+$ | $C_2H_4N^+/CH_2N_2^+/CNO^+$ | $C_2H_4N^+/CH_2N_2^+/CNO^+$ | $CH_2N_2^+/CNO^+$ |
| 43 | $C_2H_5N^+$ | $C_2H_5N^+$ | $C_2H_5N^+$ | $CHNO^+$ |
| 46 | $NO_2^+$ | $NO_2^+$ | $NO_2^+$ | $NO_2^+$ |
| 50 | $C_3N^+$ | $C_3N^+$ | $C_3N^+$ | $C_3N^+$ |
| 51 | $C_3HN^+$ | $C_3HN^+$ | $C_3HN^+$ | $C_3HN^+$ |
| 52 | $C_3H_2N^+/C_2N_2^+$ | $C_3H_2N^+/C_2N_2^+$ | $C_3H_2N^+/C_2N_2^+$ | $C_3H_2N^+/C_2N_2^+$ |
| 53 | $C_3H_3N^+/C_2HN_2$ | $C_3H_3N^+/C_2HN_2^+$ | $C_3H_3N^+/C_2HN_2^+$ | $C_2HN_2^+$ |
| 54 | $C_2H_2N_2^+/C_3H_4N^+/C_2NO^+$ | $C_2H_2N_2^+/C_3H_4N^+/C_2NO^+$ | $C_2H_2N_2^+/C_3H_4N^+/C_2NO^+$ | $C_2H_2N_2^+/C_2NO^+$ |
| 55 | $C_2H_3N_2^+/C_2HNO^+/C_3H_5N^+$ | — | $C_2H_3N_2^+/C_2HNO^+/C_3H_5N^+$ | — |
| 62 | — | $C_4N^+$ | $C_4N^+$ | — |
| 63 | — | $C_4HN^+$ | $C_4HN^+$ | — |
| 63.5 | — | $I^{++}$ | $I^{++}$ | $I^{++}$ |
| 64 | $C_3N_2^+/C_4H_2N^+$ | $C_3N_2^+/C_4H_2N^+$ | $C_3N_2^+/C_4H_2N^+$ | $C_3N_2^+/C_4H_2N^+$ |
| 65 | $C_3HN_2^+/C_4H_3N^+$ | $C_3HN_2^+/C_4H_3N^+$ | $C_3HN_2^+/C_4H_3N^+$ | $C_3HN_2^+$ |
| 66 | $C_2N_3^+/C_3H_2N_2^+/C_4H_4N^+$ | $C_2N_3^+/C_3H_2N_2^+/C_4H_4N^+$ | $C_2N_3^+/C_3H_2N_2^+/C_4H_4N^+$ | $C_3H_2N_2^+/C_2N_3^+$ |
| 67 | $C_2HN_3^+/C_3H_3N_2^+/C_4H_5N^+$ | — | $C_2HN_3^+/C_3H_3N_2^+/C_4H_5N^+$ | — |
| 68 | — | — | $C_2N_2O^+/C_2H_2N_3^+/C_3H_4N_2^+/C_4H_6N^+$ | — |
| 69 | — | $C_2HN_2O^+/C_3H_5N_2^+$ | $C_2HN_2O^+/C_3H_5N_2^+$ | $C_2HN_2O^+$ |
| 76 | — | — | $C_4N_2^+$ | — |
| 77 | — | — | $C_4HN_2^+$ | — |
| 78 | — | — | $C_3N_3^+/C_4H_2N_2^+$ | — |
| 79 | — | — | $C_3HN_3^+/C_4H_3N_2^+$ | $^{79}Br^+$ |
| 80 | — | — | $C_3N_2O^+/C_3H_2N_3^+/C_4H_4N_2^+$ | $H^{79}Br^+$ |
| 81 | — | — | $C_3HN_2O^+/C_3H_3N_3^+/C_4H_5N_2^+$ | $^{81}Br^+$ |
| 82 | $C_4H_6N_2^+$ | — | — | $H^{81}Br^+$ |
| 91 | — | — | — | $C^{79}Br^+$ |
| 93 | — | — | — | $C^{81}Br^+$ |
| 106 | — | — | — | $CH^{79}BrN^+$ |
| 108 | — | — | — | $CH^{81}BrN^+$ |
| 127 | — | $I^+$ | $I^+$ | $I^+$ |

at the N 1s, O 1s, and I 3d edges. At the C 1s edge, the differences between iodinated samples become more pronounced. $BrINimH^+$ produces on average 10.6% of $NO_2^+$ ions, $INimH^+$ produces 7.8%, and $EtINimH^+$ produces only 2.0%. Interestingly, there is an increase of 257% in $NO_2^+$ ions for $EtINimH^+$ at C 1s starting from 294.5 eV to 300 eV. As can be seen in Fig. S1, presented in the ESI,† $NO_2^+$ production increases after the ionization threshold and it becomes the third dominant ion at 298.5 eV. With the exception of $BrINimH^+$, there is an overall increase in $NO_2^+$ production from the C 1s edge to the I 3d edge for all samples. However, in the case of $BrINimH^+$, the $NO_2^+$ yield decreases from 10.6% at C 1s to 5.7% at I 3d.

**3.2.1 NEXAMS spectra at C 1s.** In Fig. 4, we present the comparison between experimental NEXAMS and calculated NEXAFS spectra at the C 1s edge for all measured samples. There is a good agreement between the experiment and theory, especially for the low-energy part of the spectra, where excitations to the lowest unoccupied orbitals occur. Different colors in the calculated spectra correspond to the contributions from the non-equivalent carbon atoms enabling the identification of their respective roles across different energy regions in the spectrum. It is expected that the incorporation of iodine mainly influences the C 1s NEXAMS as the iodine is attached to the carbon site, C3, in all samples. In addition to that, there is a different number of carbon atoms in iodinated samples that affects the shape of the C 1s NEXAMS spectra.

Comparing the C 1s NEXAMS of the iodine-free and iodinated samples, a shift of about 0.5 eV towards higher excitation energies is observed for the iodinated samples indicating a destabilization of the LUMO orbitals by the addition of iodine. For all samples, the first resonance is dominated by the transition 1s → LUMO from the carbon $C_3$, which is bound to the iodine atom, in all systems except in $NimH^+$, where it is bound to hydrogen. If in the case of a non-iodinated sample, this is the only carbon responsible for the first resonance, then in the iodinated samples, a contribution from other carbons is present and is different for different samples. Please refer to Table SI in the ESI† for the assignments of the calculated electronic transitions. In $NimH^+$ and $INimH^+$ (Fig. 4a and b), the second resonance consists mainly of the transitions 1s → LUMO in carbon C2 which is connected to $NO_2$ group. For $BrINimH^+$ and $EtINimH^+$ it is dominated by the 1s → LUMO+1, LUMO transitions from C1 that is connected to bromine or methyl group, respectively. The third resonance is the strongest for $NimH^+$ and predominantly consists of C1 contribution 1s → LUMO+1. For iodinated samples, $INimH^+$ and $EtINimH^+$, the third resonance is mostly C3 contribution 1s → LUMO+2 and

 

Table 2 Ions observed in Born–Oppenheimer-based molecular dynamics simulations from the fragmentation of protonated parent molecules after ionization and subsequent Auger decay and cascaded Auger decay. The percent indicates how often the ion appears in a simulation at the final time step

| | | NimH (%) | INimH (%) | | |
|---|---|---|---|---|---|
| *m/z* | Ions | +3 | +3 | +4 | +5 |
| 1 | $H^+$ | 30 | 40 | 60 | 80 |
| 12 | $C^+$ | 10 | 15 | 15 | 25 |
| 13 | $CH^+$ | 5 | — | — | — |
| 14 | $CH_2^+$ | — | — | — | 15 |
| 15 | $CH_3^+$/$NH^+$ | 15 | — | 15 | 5 |
| 16 | $O^+$ | 25 | 25 | 40 | 60 |
| 24 | $C_2^+$ | 5 | — | — | — |
| 25 | $C_2H^+$ | 10 | — | — | 15 |
| 26 | $C_2H_2^+$/$NC^+$ | 10 | 10 | 26 | 55 |
| 27 | $CHN^+$ | 25 | 5 | 30 | 30 |
| 28 | $CH_2N^+$ | 10 | — | — | — |
| 30 | $NO^+$ | 25 | 25 | 40 | 60 |
| 38 | $C_2N^+$ | — | — | 10 | 5 |
| 40 | $C_2H_2N^+$ | 25 | — | 5 | — |
| 41 | $C_2H_3N^+$ | — | 5 | — | 5 |
| 42 | $C_2H_4N^+$ | 40 | 25 | 30 | 40 |
| 46 | $NO_2^+$ | 65 | 50 | 55 | 40 |
| 52 | $C_3H_2N^+$ | — | — | 5 | — |
| 53 | $C_3H_3N^+$ | — | — | 5 | 15 |
| 54 | $C_2H_2N_2^+$ | 5 | — | — | — |
| 55 | $C_2H_3N_2^+$ | 5 | — | — | — |
| 65 | $C_3HN_2^+$ | — | — | — | — |
| 66 | $C_3H_2N_2^+$ | 5 | — | — | — |
| 67 | $C_3H_3N_2^+$ | — | — | — | — |
| 80 | $C_4H_4N_2^+$ | — | — | 5 | — |
| 81 | $C_4H_5N_2^+$ | — | 5 | — | — |
| 82 | NimH-$NO_2^+$ | 25 | — | — | — |
| 99 | $C_3H_3N_2O_2^+$ | 5 | — | — | — |
| 127 | $I^+$ | — | 15 | 50 | 60 |
| 139 | $CI^+$ | — | — | — | 10 |
| 154 | $CHIN^+$ | — | 10 | 5 | 10 |
| 165 | $C_2IN^+$ | — | — | 5 | 5 |
| 166 | $C_2HIN^+$ | — | 15 | 20 | 15 |
| 206 | $C_4H_3IN_2^+$ | — | — | 5 | — |
| 207 | INim-$NO_2^+$ | — | 10 | — | — |
| 208 | INimH-$NO_2^+$ | — | 25 | 15 | — |
| 253 | $INim^+$ | — | 20 | — | — |
| 254 | $INimH^+$ | — | — | — | — |

1s → LUMO+1, correspondingly, while for $BrINimH^+$, it is a mixture of C2 1s → LUMO+4 and C1 1s → LUMO+2. As shown in Fig. 3, the structural differences of the samples significantly affect the amount of $NO_2^+$ ions produced at C 1s edge. However, all of the samples show the same trend of increasing $NO_2^+$ production after the ionization threshold at about 296 eV. Above ionization energy, the contribution from the valence ionization should be taken into account. Possibly, the $NO_2^+$ separation pathway is more prominent after valence ionization. More likely, the molecule simply obtains more charge after photoionization and localization of the charge on the carbon atom seems to enhance the $NO_2^+$ production. The effect is less visible for N 1s, O 1s, and I 3d edges. In the case of N 1s and O 1s, the charge localizes on the nitro group which could lead to its consequent fragmentation. In the I 3d, a highly charged state is created due to Auger cascades that generally leads to a more vigorous fragmentation.

**3.2.2 NEXAMS spectra at N 1s and O 1s.** The O 1s and N 1s NEXAMS spectra allow following the fate of $NO_2^+$ ions when the electron transitions are occurring in the nitro group. The comparison between the experimental N 1s NEXAMS and calculated NEXAFS spectra for $NimH^+$ and $INimH^+$ is depicted in Fig. 5 and demonstrates good agreement. The experimental NEXAMS spectra at the N 1s, shown as black dotted lines, exhibit two prominent resonances at about 401.9 eV and 404.1 eV. The calculation shows the contributions of different nitrogen atoms to the spectrum. The assignments of the calculated electronic transitions are presented in Table SII in the ESI.† In both samples, the main contributions to the first peak are the transitions 1s → LUMO and 1s → LUMO+1 in the nitrogen atoms of the imidazole ring. The second peak primarily arises from 1s → LUMO transitions in the nitrogen of the nitro group.

As can be seen in Fig. 3, at the N 1s edge, there are dips in the $NO_2^+$ curves coinciding with the resonances in the NEXAMS spectra. The dip appearing at the second resonance is the strongest. Also, dips corresponding to the fifth and sixth resonances are present and are particularly strong in the non-iodinated sample. As Fig. 5 shows, nitro group nitrogen is mainly responsible for these resonances. This indicates that whenever electronic transitions are occurring from the nitro group nitrogen, the $NO_2^+$ production is suppressed. There are three main processes that could lead to the reduction in the $NO_2^+$ production. First, after photoabsorption, the nitro group can consequently dissociate into smaller fragments such as $NO^+$, $O^+$, and $N^+$. We cannot see the lower masses in the experiment but the calculation predicts the formation of $NO^+$ and $O^+$ ions (see Table 2). The second option is that following

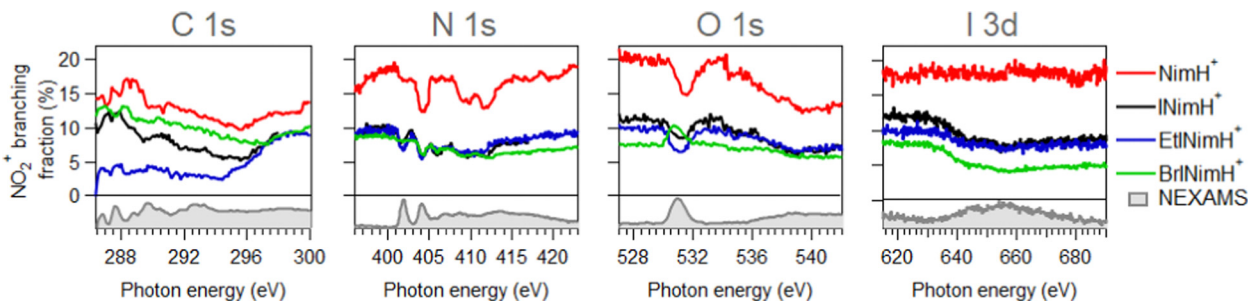


Fig. 3 Branching fraction of $NO_2^+$ ions across measured edges. Below zero, experimental NEXAMS spectra of $EtINImH^+$ are shown to guide the eye to the resonance positions.

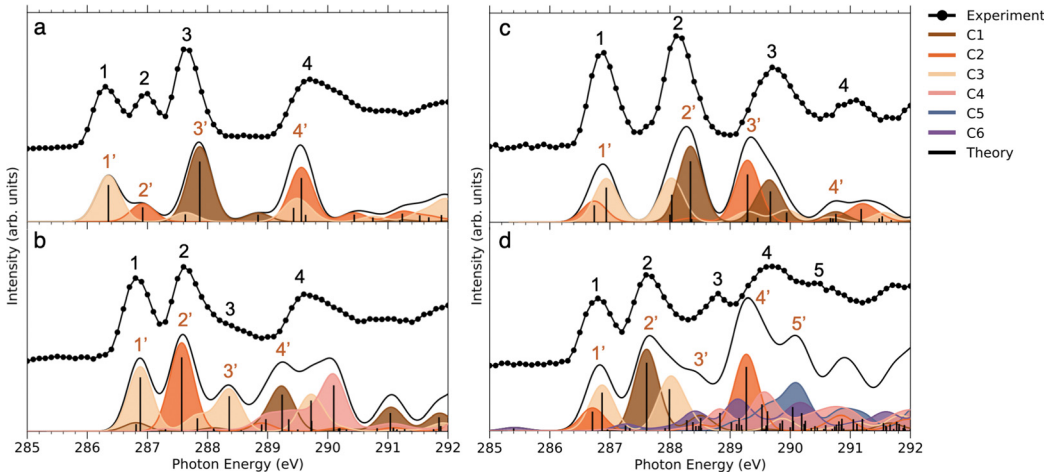


Fig. 4 NEXAFS of: (a) $NimH^+$ (b) $INimH^+$ (c) $BrINimH^+$ and (d) $EtINimH^+$ at C 1s: experiment *vs.* theory. The theoretical spectra were shifted by 10.75, 10.6, 10.5, and 10.6 eV respectively to align with the first peak of the experimental data. Different colors indicate contributions to the total spectra from separate carbons. The spectrum has been obtained by individual transition probabilities and convoluted by a Gaussian function with FWHM of 0.5 eV.

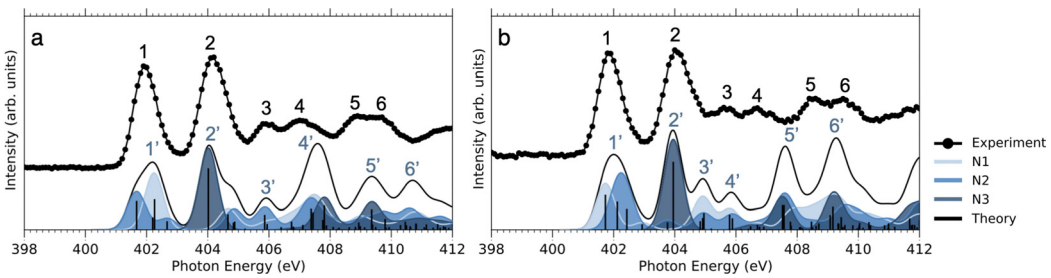


Fig. 5 NEXAFS of (a) $NimH^+$ and (b) $INimH^+$ at N 1s. The theoretical spectra were shifted by 12.3 eV to align with the first resonance peak in the experimental data. Different shades of blue indicate contributions to the total spectra from the three nitrogen atoms. Each bar represents one transition. The bar graph has been convoluted using a Gaussian function with an FWHM of 0.7 eV to better fit the experimental spectrum.

electronic relaxation after photoabsorption the nitro group ejects as a neutral. Finally, the most unlikely option is that the bond between the nitro group and the imidazole ring does not dissociate after photoabsorption.

At the O 1s edge, a reduction of the $NO_2^+$ ions at the resonance around 531.0 eV is observed for all the samples except for $BrINimH^+$, in which $NO_2^+$ production is increased. The behavior observed suggests that there might be different fragmentation pathways leading to the production of $NO_2^+$ ions following core excitations of oxygen atoms in the nitro group. These pathways appear to be influenced by the structural differences among the molecules studied. The fact that $NO_2^+$ production is increased in the case of $BrINimH^+$ at the O 1s edge suggests that the presence of bromine instead of the methyl group at the C1 site in the molecule could affect the fragmentation process, leading to a different behavior compared to the other studied samples.

**3.2.3 NEXAMS spectra at I 3d.** For all iodinated samples, we observe a decrease in the production of $NO_2^+$ ions after the photoabsorption onset at the I 3d edge, which appears approximately at 645.6 eV as shown in Fig. 3. Due to the absence of a heavy element absorption hotspot, the non-iodinated sample shows no change in $NO_2^+$ production across the I 3d edge. Across the I 3d edge, the atomic fragments such as $I^+$, $Br^+$, and $I^{++}$ gain significant intensity (see Fig. S4 in ESI†). For $INimH^+$, there is an increase of $I^+$ and $I^{++}$ ions, while for $BrINimH^+$, $Br^+$ and $I^{++}$ ions are predominantly produced. For the $EtINimH^+$ sample, ions at $m/z$ 38 ($C_2N^+$) and 51 ($C_3HN^+$) show the strongest gain in intensity. One would expect to observe a higher degree of atomization of the molecules with a high-$z$ hotspot at I 3d photon energies due to the creation of highly charged final states as a result of Auger cascades. This is confirmed by our calculation results presented in Table 2, where we see an increase in the intensity of $H^+$, $C^+$, $O^+$, and $I^+$ ions at higher charges. A higher degree of atomization could explain the decrease in the production of $NO_2^+$ fragment above 640 eV due to its further possible fragmentation into $N^+$, $O^+$, and $NO^+$.

### 3.3 Molecular dynamics

Fig. 6 shows the first four virtual molecular orbitals for the different molecules studied. LUMO is primarily located close to the nitro group in all four molecules, with bonding features between N3 and C2. LUMO+1, LUMO+2, and LUMO+3 all share

 

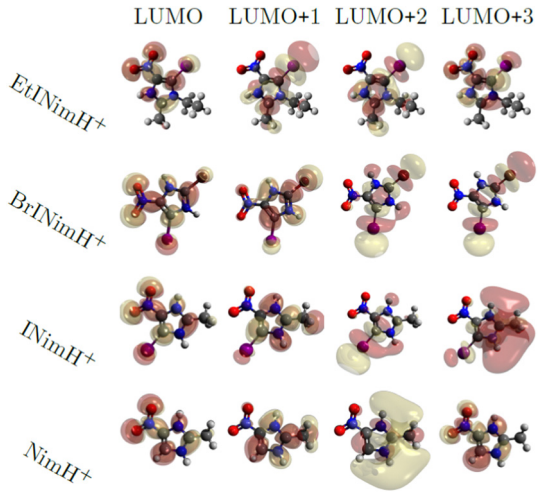


Fig. 6 Visualization of molecular orbitals representing the first four unoccupied states using an isovalue of 0.02.

the weight of the orbitals mainly delocalized at the imidazole ring. Due to the similarity in orbital localization for the different molecules, one would expect the produced fragments by photoabsorption to be created in a similar way, regardless of the addition of heavy atoms or functional groups to the ring, which also can be observed in the overall representation of measured fragments in Fig. 2. The disparity between the LUMO levels, however, would indicate the production of distinctive fragments at increasing photon energies. This is not the case, as seen across the different measured edges in Fig. 2, thus the electronic relaxation occurs before fragmentation, a phenomenon observed in earlier studies.[44]

Now we turn to the result of the calculations performed with time-resolved molecular dynamics on $NimH^+$ and $INimH^+$ above the ionization threshold. The charged molecular system is assumed to stay in its electronic ground state at a high temperature and is allowed to freely propagate through the fragmentation process. In relation to the experiment, an electron has been ionized from a 1s or 3d orbital in the protonated molecule causing the emittance of one, two, or three Auger electrons. The produced fragments obtained at the studied charge states are presented in Table 2. We can observe significantly higher rates of low-mass fragments originating from the iodinated sample in contrast to the non-iodinated molecule arising from C–H bond dissociation and thereafter opening of the nitroimidazole ring, a similar behavior recognized in other carbon-based aromatic molecules.[47] The channel which leads to an open ring has previously been observed as a high energy path upon NO and $NO_2$ production.[48]

An interesting feature is a high production of $NO^+$ and $NO_2^+$ fragments appearing during irradiation of both iodinated and non-iodinated molecules. The $NO^+$ ion is outside the measurable area in the experiment but is conspicuously produced at 25 to 60% of the simulations depending on the molecule and the charge. Being an important part of the suggested oxygen mimetics mechanism, their rate of production is important to be understood.

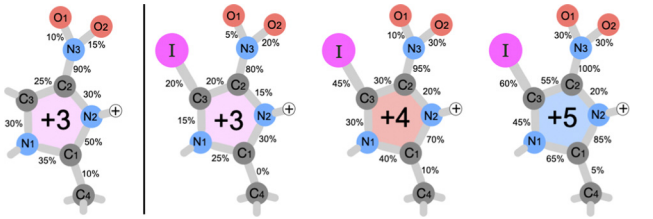


Fig. 7 Percentage of broken bonds between each atom except for hydrogen in triply-, quadruply- and quintuply-charged protonated INimH and triply-charged NimH molecules noted in the dynamics simulations.

For further analysis of the bond sensitivity in relation to observed fragments, we present the percent of broken bonds between all atoms heavier than hydrogen in Fig. 7. As one can observe, the nitroimidazole ring does, to a large extent, share the bond breaking evenly for the $NimH^{3+}$ system, supporting the experimental yield observed in Fig. 2. If the charge increases through the Auger cascade, a higher emphasis is laid on the C2–C3 bond and nitrogen bonds connected to C1. In both cases, the N3–C2 bond is close to 100%, leaving this bond to be the weakest in the system. Only small changes in breaking probability can be noticed after introducing an iodine atom to the ring as seen in the percentages for the $INim^{3+}$ and $INim^{4+}$ structures. In addition to the production of analogous products, it appears that there might be a potential tendency towards a shorter lifetime of the N3–C2 bond in the iodine-enhanced sample when subjected to irradiation at energies near the I 3d edge (see Table SIII in the ESI†). This could open for a more localized radiation treatment using INim while maintaining sufficiently high $NO_2^+$ production. However, it is important to note that these observations may be influenced by low statistics and further studies with larger data sets are required to gain a more comprehensive understanding of the potential impact on the lifetime of the N3–C2 bond due to heavy element incorporation.

## 4 Conclusion

We have applied ion TOF spectroscopy combined with synchrotron radiation to experimentally study the production of radiosensitization-relevant $NO_2^+$ ions in iodinated ($INimH^+$, $EtINimH^+$, $BrINimH^+$) and non-iodinated ($NimH^+$) nitroimidazoles at various photon energies. The key findings are (i) the samples display minimal fluctuations in resulting fragments across C 1s, N 1s, O 1s, and I 3d edges, indicating consistent fragmentation patterns despite variations in absorption sites; (ii) in terms of $NO_2^+$ production, the non-iodinated molecule consistently produced the highest amount of $NO_2^+$ ions upon core excitation and ionization across all measured edges. The addition of iodine to the sample on average lowered the production of $NO_2^+$ ions by about 50% in comparison to the iodine-free nitroimidazole across N 1s, O 1s, and I 3d edges. For the C 1s edge, the amount of produced $NO_2^+$ highly depended on the sample and $BrINimH^+$ showed the best result in comparison to $NimH^+$ (lower by 26%), while $EtINimH^+$ demonstrated the

worst result (lower by 86%); (iii) electronic transitions from the N 1s with the participation of the nitro group nitrogen result in the suppression of $NO_2^+$ production, indicating a strong site-specific fragmentation effect for all samples.

We observed similar trends in the fragmentation of iodinated and non-iodinated samples across various photon energies. Although the production of sensitization-relevant $NO_2^+$ ions is lower in the iodinated samples, there is a release of $I^+$ and $I^{++}$ ions, which also could be damaging to the cancerous cells. Therefore, iodinated nitroimidazoles seem to maintain high levels of production of damaging fragments upon fragmentation. Considering the possibility of additional local damage through Auger cascades due to the presence of the heavy atom, halogenation of nitroimidazoles could be a promising strategy for developing more effective radiosensitizers. However, further *in vitro* investigations are necessary to validate the clinical applicability of these molecules. Moreover, exploring the influence of water, a prominent molecule in cellular environments, on nitroimidazole fragmentation is essential for more accurate comparisons with *in vivo* conditions.

## Author contributions

Conceptualization, MB; experiments, MB, PHWS, IU, LS, ALV; computation and software, PHWS, OG, NT, CC; experimental data analysis, MB, ALV; calculations analysis, PHWS, NT, OG, CC; writing of the manuscript, MB, PHWS; review and editing, OB, VZB, KH, MT, RL, CC, NT, OG; funding acquisition, MB. All authors have read and agreed to the final version of the manuscript.

## Conflicts of interest

There are no conflicts to declare.

## Acknowledgements

This work was supported by the Estonian Research Council grant (MOBTP1013). We acknowledge the BESSY II synchrotron facility for the granted time at the Nanocluster Trap end-station of the UE52_PGM beamline. We acknowledge the Swedish Research Foundation for Strategic Research, the Swedish Research Council (2017-05128, 2018-00740, 2019-03935), the Swedish Research Council *via* the Röntgen-Ångstöm Cluster, program-oriented funds of the Helmholtz Association. The computations were enabled by resources provided by the Swedish National Infrastructure for Computing (SNIC) at Linköping University in the projects 2022/1-36 and 2022/22-597. L. S. acknowledges funding from the Helmholtz Initiative and Networking Fund. This article is based upon work from COST Action CA18212 – Molecular Dynamics in the GAS phase (MD-GAS), supported by COST (European Cooperation in Science and Technology).

## Notes and references

1 H. Murshed, *Fundamentals of Radiation Oncology*, 3rd edn, 2019.
2 G. E. Adams, I. R. Flockhart, C. E. Smithen, I. J. Stratford, P. Wardman and M. E. Watts, *Radiat. Res.*, 1976, **67**, 9–20.
3 S. Rey, L. Schito, M. Koritzinsky and B. G. Wouters, *Adv. Drug Delivery Rev.*, 2017, **109**, 45–62.
4 G. H. Harrison and J. Wright, in *Cancer Management in Man: Detection, Diagnosis, Surgery, Radiology, Chronobiology, Endocrine Therapy*, ed. A. L. Goldson, Springer Netherlands, Dordrecht, 1989, pp. 170–178.
5 J. F. Fowler, G. E. Adams and J. Denekamp, *Cancer Treat. Rev.*, 1976, **3**, 227–256.
6 A. Zahoor, M. V. Lafleur, R. C. Knight, H. Loman and D. I. Edwards, *Biochem. Pharmacol.*, 1987, **36**, 3299–3304.
7 H. Wang, X. Mu, H. He and X.-D. Zhang, *Trends Pharmacol. Sci.*, 2018, **39**, 24–48.
8 B. T. Oronsky, S. J. Knox and J. J. Scicinski, *Transl. Oncol.*, 2012, **5**, 66–71.
9 P. Sonveaux, B. F. Jordan, B. Gallez and O. Feron, *Eur. J. Cancer*, 2009, **45**, 1352–1369.
10 S. Pandeti, L. Feketeová, T. J. Reddy, H. Abdoul-Carime, B. Farizon, M. Farizon and T. D. Märk, *RSC Adv.*, 2017, **7**, 45211–45221.
11 *Radiation Damage in Biomolecular Systems*, ed. G. García Gómez-Tejedor and M. C. Fuss, Springer Netherlands, Dordrecht, 2012.
12 W. Krause, A. Jordan, R. Scholz and J.-L. M. Jimenez, *Anticancer Res.*, 2005, **25**, 2145–2151.
13 R. Santos Mello, H. Callisen, J. Winter, A. R. Kagan and A. Norman, *Med. Phys.*, 1983, **10**, 75–78.
14 A. Joubert, M.-C. Biston, C. Boudou, J.-L. Ravanat, T. Brochard, A.-M. Charvet, F. Estève, J. Balosso and N. Foray, *Int. J. Radiat. Oncol., Biol., Phys.*, 2005, **62**, 1486–1496.
15 F. Kajfež, L. Klasinc and V. Šunjić, *J. Heterocycl. Chem.*, 1979, **16**, 529–531.
16 P. Bolognesi, A. R. Casavola, A. Cartoni, R. Richter, P. Markus, S. Borocci, J. Chiarinelli, S. Tošić, H. Saadeh, M. Masič, B. Marinković, K. Prince and L. Avaldi, *J. Chem. Phys.*, 2016, **145**, 191102.
17 J. Chiarinelli, A. R. Casavola, M. C. Castrovilli, P. Bolognesi, A. Cartoni, F. Wang, R. Richter, D. Catone, S. Tosic, B. P. Marinkovic and L. Avaldi, *Front. Chem.*, 2019, **7**, 1–14.
18 P. Bolognesi, V. Carravetta, L. Sementa, G. Barcaro, S. Monti, P. Manjari Mishra, A. Cartoni, M. C. Castrovilli, J. Chiarinelli, S. Tosic, B. P. Marinkovic, R. Richter and L. Avaldi, *Front. Chem.*, 2019, **7**, 151.
19 L. Feketeová, O. Plekan, M. Goonewardane, M. Ahmed, A. L. Albright, J. White, R. A. J. OHair, M. R. Horsman, F. Wang and K. C. Prince, *J. Phys. Chem. A*, 2015, **119**, 9986–9995.
20 E. Itälä, K. Tanzer, S. Granroth, K. Kooser, S. Denifl and E. Kukk, *J. Mass Spectrom.*, 2017, **52**, 770–776.
21 A. Cartoni, A. R. Casavola, P. Bolognesi, M. C. Castrovilli, D. Catone, J. Chiarinelli, R. Richter and L. Avaldi, *J. Phys. Chem. A*, 2018, **122**, 4031–4041.

22 E. Itälä, H. Myllynen, J. Niskanen, J. González-Vázquez, Y. Wang, D. T. Ha, S. Denifl and E. Kukk, *J. Phys. Chem. A*, 2019, **123**, 3074–3079.
23 E. Itälä, J. Niskanen, L. Pihlava and E. Kukk, *J. Phys. Chem. A*, 2020, **124**, 5555–5562.
24 M. Satta, A. R. Casavola, A. Cartoni, M. C. Castrovilli, D. Catone, J. Chiarinelli, S. Borocci, L. Avaldi and P. Bolognesi, *ChemPhysChem*, 2021, **22**, 2387–2391.
25 R. Flammang, J. Elguero, H. Thanh Le, P. Gerbaux and M. Tho Nguyen, *Chem. Phys. Lett.*, 2002, **356**, 259–266.
26 K. Tanzer, L. Feketeová, B. Puschnigg, P. Scheier, E. Illenberger and S. Denifl, *Angew. Chem., Int. Ed.*, 2014, **53**, 12240–12243.
27 L. Feketeová, J. Postler, A. Zavras, P. Scheier, S. Denifl and R. A. J. O'Hair, *Phys. Chem. Chem. Phys.*, 2015, **17**, 12598–12607.
28 R. Meißner, J. Kočišek, L. Feketeová, J. Fedor, M. Fárník, P. Limão-Vieira, E. Illenberger and S. Denifl, *Nat. Commun.*, 2019, **10**, 2388.
29 R. Meißner, L. Feketeová, A. Bayer, P. Limão-Vieira and S. Denifl, *J. Chem. Phys.*, 2021, **154**, 074306.
30 L. Pihlava, M. Berholts, J. Niskanen, A. Vladyka, K. Kooser, C. StrÅhlman, P. Eng-Johnsson, A. Kivimäki and E. Kukk, *Phys. Chem. Chem. Phys.*, 2023, **25**, 13004–13011.
31 A. Yokoya and T. Ito, *Int. J. Radiat. Biol.*, 2017, **93**, 743–756.
32 S. McGregor, J. Minni and D. Herold, *J. Clin. Aesthetic Dermatol.*, 2015, **8**, 12–14.
33 R. Vinit, R. Amit, S. Saurabh, M. Raghvendra, M. Ravindra, P. Piyush, G. Ankur and S. Mahendra, *J. Anal. Pharm. Res.*, 2018, **7**, 175–180.
34 K. Hirsch, J. T. Lau, P. Klar, A. Langenberg, J. Probst, J. Rittmann, M. Vogel, V. Zamudio-Bayer, T. Möller and B. V. Issendorff, *J. Phys. B: At., Mol. Opt. Phys.*, 2009, **42**, 154029.
35 P. J. Stephens, F. J. Devlin, C. F. Chabalowski and M. J. Frisch, *J. Phys. Chem.*, 1994, **98**, 11623–11627.
36 F. Neese, F. Wennmohs, U. Becker and C. Riplinger, *J. Chem. Phys.*, 2020, **152**, 224108.
37 E. van Lenthe, A. van der Avoird and P. E. S. Wormer, *J. Chem. Phys.*, 1998, **108**, 4783–4796.
38 E. K. Gross and W. Kohn, *Adv. Quantum Chem.*, 1990, **21**, 255.
39 J. M. Soler, E. Artacho, J. D. Gale, A. Garca, J. Junquera, P. Ordejón and D. Sánchez-Portal, *J. Phys.: Condens. Matter*, 2002, **14**, 2745.
40 O. Grånäs, N. Timneanu, I. Eliah Dawod, D. Ragazzon, S. Trygg, P. Souvatzis, T. Edvinsson and C. Caleman, *J. Chem. Phys.*, 2019, **151**, 144307.
41 I. Eliah Dawod, N. Timneanu, A. P. Mancuso, C. Caleman and O. Grånäs, *Phys. Chem. Chem. Phys.*, 2022, **24**, 1532–1543.
42 O. GrÅnäs, A. Mocellin, E. S. Cardoso, F. Burmeister, C. Caleman, O. Björneholm and A. N. de Brito, *J. Phys. B: At., Mol. Opt. Phys.*, 2020, **53**, 244007.
43 C. Caleman, F. Junior, O. Granas and A. Martin, *Crystals*, 2020, **10**, 585.
44 G. Gopakumar, P. H. Svensson, O. Grånäs, B. Brena, L. Schwob, I. Unger, C.-M. Saak, M. Timm, C. Bülow and M. Kubin, *et al.*, *J. Phys. Chem. A*, 2022, **126**, 1496–1503.
45 J. P. Perdew, K. Burke and M. Ernzerhof, *Phys. Rev. Lett.*, 1996, **77**, 3865–3868.
46 N. Troullier and J. L. Martins, *Phys. Rev. B: Condens. Matter Mater. Phys.*, 1991, **43**, 1993–2006.
47 S. Oghbaie, M. Gisselbrecht, E. P. MÅnsson, J. Laksman, C. StrÅhlman, A. Sankari and S. L. Sorensen, *Phys. Chem. Chem. Phys.*, 2017, **19**, 19631–19639.
48 M. Satta, A. R. Casavola, A. Cartoni, M. C. Castrovilli, D. Catone, J. Chiarinelli, S. Borocci, L. Avaldi and P. Bolognesi, *ChemPhysChem*, 2021, **22**, 2387–2391.